23 European Conference on Fracture – ECF23

A novel FFT-based homogenization scheme for cohesive zones

Felix Bödeker[a,*], Pauline Herr[a], Ramin Moshfegh[b], Anders Biel[c], Stephan Marzi[a]

[a]*Technische Hochschule Mittelhessen, Wiesenstraße 14, 35390 Gießen, Germany*
[b]*Lamera AB, A Odhners gata 17, 421 30 Västra Frölunda, Sweden*
[c]*Karlstad University, Universitetsgatan 2, 651 88 Karlstad, Sweden*

Abstract

Cohesive Zone Models with finite thickness are widely used for the fracture mechanical modeling of layers of material, e.g., adhesives. Within this approach, the whole layer is modeled as a Cohesive Zone. Moreover, computational homogenization techniques are crucial for the development of advanced engineering materials, which are often heterogeneous. Compared to the classical Finite Element Method (FEM), computationally more efficient solvers based on the Fast Fourier Transform (FFT) are expected to reduce the computational effort needed for the homogenization. Originated from an existing method for the computational homogenization of Cohesive Zones using FEM, a novel FFT-based homogenization scheme for Cohesive Zone Models was developed. Our implementation of the FFT solver uses the Barzilai-Borwein scheme and a non-local ductile damage model for the fracture behavior. Finally, the method is applied to the core material of Hybrix™ metal sandwich plates, and the good agreement with experimental results in opening mode I is shown.

Keywords: Computational Homogenization; Cohesive Zone Modeling; Hybrix™

1. Introduction

Cohesive Zone Models (CZM) are often used to model the (macroscopic) fracture behavior of materials. In some cases, it is also useful to treat layers of material as a finite thickness Cohesive Zone (CZ), whereby the whole thickness of the layer is described by the CZM. Nevertheless, it should be mentioned that this approach is a strong simplification of the reality as deformation and stresses in through thickness direction are considered only. Hence, the displacement jumps (separation vector) and possible additional internal state variables are mapped to the traction vector by the constitutive law. The approach is typically used to model the fracture behavior of adhesive layers, e.g., in Bödeker and Marzi (2020), but in this work we also use it for the porous, polymeric fiber-binder core of a sandwich plate with metal face sheets called Hybrix™ by the manufacturer Lamera AB, cf. Section 4. The required Traction Separation

---

* Corresponding author. Tel.: +49-641-309-2230 ; fax: +49-641-309-2905.
E-mail address: felix.boedeker@me.thm.de

Laws (TSL) can be measured directly from experiments, e.g., using Double Cantilever Beam (DCB) tests in mode I. Nevertheless, a full experimental characterization of the mechanical behavior is still time-consuming and costly.

The importance of complex composite materials for structural applications is increasing in many industries. For a systematic and less time-consuming development process of such advanced composites, it is crucial to link the mechanical properties of the constituents, composition, and geometry of the microstructure to the macroscopic mechanical properties of the material.

For this purpose, several homogenization techniques have been developed to reduce the experimental effort. Besides the analytical mean field approaches, which are more suited to comparably simple microstructure geometries, computational approaches gained in importance in recent years owing to the increasing computational power available. In this method, virtual Representative Volume Elements (RVE) for the microstructure of the materials of interest are generated and used for the computations. This also allows for the virtual development of advanced composite materials.

The computational homogenization techniques are often based on FEM; however, the Fast Fourier Transform (FFT)-based homogenization is a promising more recent method which is expected to allow for a reduction in computational costs compared to FEM in many applications, cf. Lucarini and Segurado (2019). Based on the pioneer work by Moulinec and Suquet (1998) the FFT-based homogenization has been significantly improved over the years using different discretization methods, e.g., finite differences and FEM, and advanced solution schemes. Furthermore, the method has been extended to homogenization problems including non-local damage and phase field fracture models. An overview of the discretization methods and solution schemes, as well as applications of the FFT-based homogenization, is given in the work by Schneider (2021). Nevertheless, FFT simulations can be performed on uniform grids only, s.t. voxelized RVEs are required as input.

In contrary to FEM (Matouš et al. (2008)), there is no homogenization method for CZM in the FFT-based framework available in the literature yet. Therefore, such an FFT-based homogenization scheme to allow for the prediction of (macroscopic) CZMs from the mechanical properties of the constituents, composition, and geometry of the microstructure was developed in this work.

The paper is structured as follows: In the first section, the FFT-based micromechanics solver including the non-local damage model is presented. Then the FFT-based homogenization method for CZM is introduced and the method is applied to the Hybrix^{TM} core layer in Section 4. A short summary of the results of this work and future perspectives are given in the final section of this paper. We represent vectors as $\vec{\bullet}$, 2nd order tensors as $\underline{\bullet}$ and 4th order tensors $\underline{\underline{\bullet}}$. $\widehat{\bullet}$ denotes the Fourier transform of a variable, whereas the volumetric average over the RVE volume V is denoted as $\frac{1}{V} \int_V \bullet \, \mathrm{d}\vec{x} = \langle \bullet \rangle_V$. The symmetric gradient operation $\frac{1}{2}\left[\mathrm{grad}\,\vec{\bullet} + (\mathrm{grad}\,\vec{\bullet})^T\right]$ is abbreviated by the symbol $\mathrm{grad}^S\,\vec{\bullet}$.

2. FFT-based homogenization

The basic concept of scale separation for the continuum homogenization is visualized in Figure 1a. At the macroscale the material is considered to be homogeneous, whereas the heterogenity appears at the microscale only. It is usually assumed that the typical length scale of the macroscale is significantly larger than the one at the microscale. The macroscale often refers to structural simulations, where the standard system of equations is usually solved by FEM. The homogenization problem, the system of equations at the microscale, is given by

$$\begin{cases} \underline{\sigma}(\vec{x})\text{ computed from constitutive law} \\ \mathrm{div}\,\underline{\sigma}(\vec{x}) = \vec{0} \\ \underline{\varepsilon}(\vec{u}^*(\vec{x})) = \underline{E} + \mathrm{grad}^S\,\vec{u}^*(\vec{x}) \\ \text{periodic boundary conditions,} \end{cases} \tag{1}$$

cf. Moulinec and Suquet (1998). It is formed by the constitutive law, the balance of momentum (static and without body forces), the strain compatibility and the periodic boundary conditions. The strain field is thereby decomposed into a volumetric average part $\underline{E}$ and a fluctuation part, that originates from the fluctuation displacement field $\vec{u}^*$.
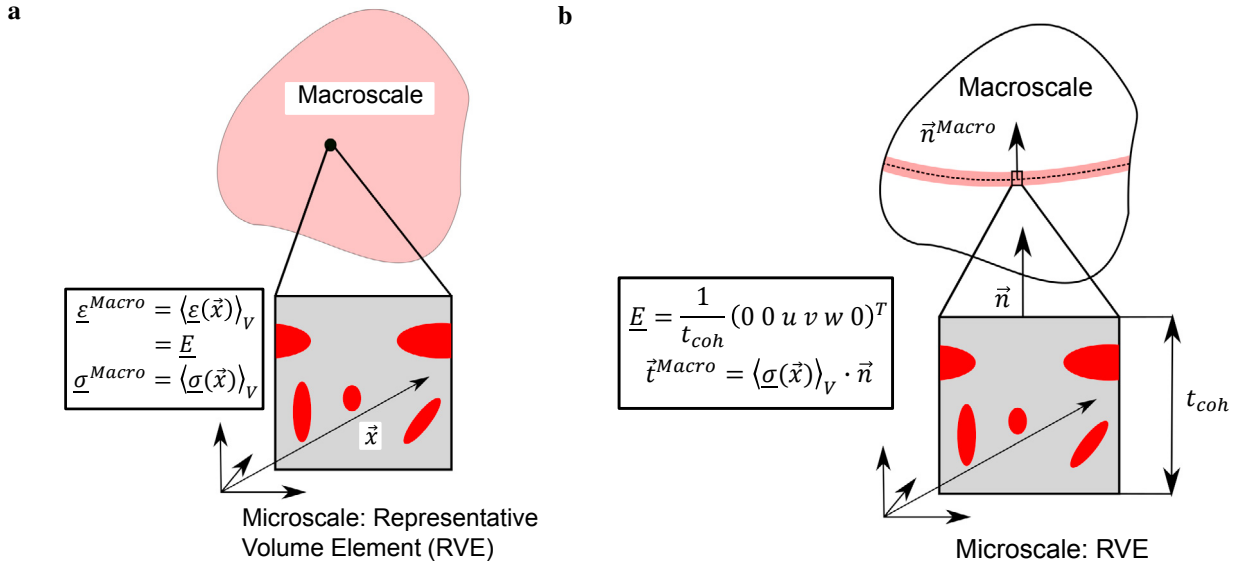
a

b

Fig. 1. (a) Concept of scale separation and homogenization for continua.; (b) Concept of scale separation and homogenization for Cohesive Zones.

The system of equations can be reformulated into the Lippmann-Schwinger equation (Moulinec and Suquet (1998)). For this purpose, the linear elastic reference material with stiffness $\underline{\underline{C}}^0$ is introduced and Equation 1 is solved for the strain field, which yields the Lippmann-Schwinger equation

$$\underline{\varepsilon} = \underline{E} - \underline{\underline{\Gamma}}^0 : \left(\underline{\sigma} - \underline{\underline{C}}^0 : \underline{\varepsilon} \right). \tag{2}$$

The spatial dependencies are neglected for notational clarity here. $\underline{\underline{\Gamma}}^0$ denotes the Green operator, which is explicitly known in Fourier space and its exact form depends on the type of discretization that is chosen, cf. Schneider (2021). In this paper, we use the staggered grid finite difference discretization from Schneider et al. (2016).

Moulinec and Suquet (1998) proposed to solve Equation 2 with the basic scheme, which can be understood as a projected gradient descent if the linear elastic reference material is set to $\underline{\underline{C}}^0 = \frac{1}{s}\underline{I}$. s denotes the step size of the gradient descent, whereas $\underline{I}$ represents the 2nd order symmetric identity tensor. The fastest convergence rate is obtained for $s = \frac{2}{\alpha_+ + \alpha_-}$, where α_+ and α_- are the largest and the smallest positive eigenvalue of the tangent stiffness matrices of all materials in the RVE. The basic scheme is usually not fast enough for most applications and therefore improved, faster algorithms have been developed. For this work, we use the Barzilai-Borwein scheme, which was introduced in Barzilai and Borwein (1988) and in Schneider (2019) in the context of FFT-based homogenization. In contrary to the basic scheme, the step size is updated every iteration within this scheme. The algorithm is summarized in Algorithm 1, where $\vec{\xi}$ represents the frequency vector in Fourier space. An extrapolation of the previous strain fields is usually used instead of $\underline{E}$ in the initialization step for higher load steps.

The Barzilai-Borwein scheme is straightforward to implement, requires comparably little memory and is very competitive regarding the computational times and convergence, but the residual does not decline monotonously. Moreover, the $\underline{\underline{\Gamma}}$ operator can be partly applied in the real space as well, which is done in our implementation. Then, only the fluctuation displacement field is Fourier transformed, s.t. the number of Fourier transforms reduces from six to three. For more details regarding the displacement-based variants of FFT solvers, we refer to Schneider et al. (2016) and Schneider (2021), as it is out of the scope of this paper.

Usually the volumetric average strain in the RVE $\langle \underline{\varepsilon}(\vec{x}) \rangle_V = \underline{E}$ is prescribed. The macro-to-micro scale transition is typically established by setting $\underline{E}$ equal to the macroscopic strain $\underline{\varepsilon}^{Macro}$, whereas at the micro-to-marco coupling

---

Algorithm 1 Barzilai-Borwein scheme

1: **Initialize:** $\underline{\varepsilon}^1 = \underline{E}$, $i = 0$ and $s^1 = \frac{2}{\alpha_+ + \alpha_-}$

2: **Iterate:** $i = i + 1$ **until convergence:**

3:   compute $\underline{\sigma}^i$ from $\underline{\varepsilon}^i$ and state variables ▹ constitutive law

4:   **if** $i > 1$ **then** $s^i = \left(1 - \frac{\langle \underline{\sigma}^i : d\underline{\varepsilon}^{i-1}\rangle_V}{\langle d\underline{\varepsilon}^{i-1} : d\underline{\varepsilon}^{i-1}\rangle_V}\right)^{-1} s^{i-1}$ ▹ update step size

5:   $\widehat{\underline{d\varepsilon}}^i = \begin{cases} \underline{0}, & \text{for } \vec{\xi} = \vec{0} \\ \underline{\hat{\underline{\Gamma}}} : \text{FFT}\left(\underline{\sigma}^i\right), & \text{else} \end{cases}$ ▹ apply Green operator

6:

7:   $\underline{\varepsilon}^{i+1} = \underline{\varepsilon}^i - s^i \text{FFT}^{-1}\left(\widehat{\underline{d\varepsilon}}^i\right)$ ▹ update strain field

---

via the stress tensor $\langle \underline{\sigma}(\vec{x})\rangle_V = \underline{\sigma}^{Macro}$ follows from the energetic consistency, the Hill-Mandel condition (Matouš et al. (2017)). The scale transition relations are also summarized in Figure 1a.

2.1. Damage model

A non-local, ductile, implicit gradient damage model is used to model the fracture behavior at the microscale in this work, which is described by

$$p_{nl} - l^2 \Delta p_{nl} = p_l, \tag{3}$$

neglecting the spatial dependencies again for notational clarity, cf. Magri et al. (2021). The non-local equivalent plastic strain p_{nl} is thereby regularized by a Helmholtz-type equation with the local equivalent plastic strain p_l as source term. The damage field is distributed within a certain localization region, whose size is related to the characteristic internal length l. Furthermore, the evolution equation for the scalar damage variable D is given by

$$D = \begin{cases} 0, & \text{for } p_{nl} < p_{nl}^0 \\ \frac{p_{nl} - p_{nl}^0}{p_{nl}^f - p_{nl}^0}, & \text{for } p_{nl}^0 \le p_{nl} < p_{nl}^f \\ 1, & \text{for } p_{nl} \ge p_{nl}^f \end{cases} \tag{4}$$

with initiation parameter p_{nl}^0 and failure parameter p_{nl}^f. In addition, the stress is computed as

$$\underline{\sigma} = (1 - D)\,\bar{\underline{\sigma}}, \tag{5}$$

where $\bar{\underline{\sigma}}$ is the undamaged, effective stress from standard von Mises plasticity.

The damage model is valid in the damaging phase only; however, in FFT-based methods we need an equation that is valid in the whole RVE owing to the Fourier transform. Following Magri et al. (2021) the Helmholtz-type equation 3 is modified to

$$p_{nl} - \text{div}\left[l^2(\vec{x})\,\text{grad}\,p_{nl}\right] = p_l \tag{6}$$

with a nonuniform characteristic length. It can be easily seen that Equation 6 reduces to Equation 3 in case of an uniform characteristic length parameter. Similar to the linear elastic reference material, a reference characteristic length l_0 is introduced according to the work by Sharma et al. (2018). Then Equation 6 is solved for p_{nl} using the FFT and fixed-point iteration, cf. Algorithm 2 line 3 and 4. More sophisticated algorithms could be used here as well; however, it was observed that the time needed for the solution of the damage problem is negligible compared to the time spent in the mechanics solver. The characteristic length parameter within the non-damaging phase is set significantly lower than the one in the damaging phase in order to avoid that the non-local equivalent plastic strain field diffuses into the non-damaging phase. We refer to Magri et al. (2021) for more details regarding the boundary conditions at the interface of damaging and non-damaging phases.

Algorithm 2 Staggered solution algorithm of the coupled problem

1: **Until convergence:**
2:   Solve Equation 1 using Algorithm 1 and obtain p_l ▷ keep p_{nl} constant
3:   **Initialize:** $j = 0$ and use p_{nl} from previous load step for p_{nl}^1
4:   **Iterate** $j = j + 1$ **until convergence:** ▷ keep p_l constant
5:     $p_{nl}^{j+1} = \text{FFT}^{-1} \dfrac{\left(\widehat{p_l} + i\vec{\xi}\cdot\text{FFT}\left(\left[l^2 - l_0^2\right]\text{FFT}^{-1}\left(i\vec{\xi}\hat{p}_{nl}^j\right)\right)\right)}{1 + l_0^2\vec{\xi}\cdot\vec{\xi}}$

The coupled problem is then solved in a staggered fashion, as also shown in Algorithm 2. It was implemented as Fortran code and the parallelization was realized using the OpenMP library (Menon and Dagum (1998)) and the FFTW library (Frigo and Johnson (2005)) for the execution of the FFTs.

3. FFT-based homogenization for cohesive zone modeling

The principle of scale separation and homogenization for Cohesive Zones is depicted in Figure 1b. In contrast to the standard homogenization for continua, only the red layer of thickness t_{coh}, which is oriented in the direction $\vec{n}^{Macro}$, is homogenized. Furthermore, the RVE also has the full thickness of the Cohesive Zone now. As already mentioned in the introductory section 1, the kinematics of a Cohesive Zone is described by displacement jumps from one interface of the layer with the surrounding body to the other one. They are summarized in the (macroscopic) separation vector $\vec{\delta} = (u\ v\ w)^T$, whose entries correspond to mode I, II and III. Following Matouš et al. (2008), without loss of generality the average strain in the Cohesive Zone is approximated by $\underline{E} = (0\ 0\ u/t_{coh}\ v/t_{coh}\ w/t_{coh}\ 0)^T$ for an orientation of the Cohesive Zone at the microscale $\vec{n}$ in z-direction, whereby Voigt notation is used for $\underline{E}$. A constant displacement field at the interfaces of the Cohesive Zone is required to describe the displacement jump. Therefore, the fluctuation displacements must be zero there, and we arrive at

$$\begin{cases} \underline{\sigma}(\vec{x})\ \text{computed from constitutive law} \\ \text{div}\,\underline{\sigma}(\vec{x}) = \vec{0} \\ \underline{\varepsilon}(\vec{u}(\vec{x})) = \underline{E} + \text{grad}^S\,\vec{u}^*(\vec{x}) \\ \vec{u}^* = \vec{0}\ \text{at the CZ interface and periodic boundary conditions elsewhere} \end{cases} \tag{7}$$

from Equation 1. However, the FFT solver presented in the section before can only deal with periodic boundary conditions, but the zero fluctuation displacement boundary condition at the interface can be approximated by adding thin layers that have a significantly higher stiffness than the material in the RVE. An example is given in Figure 3 for a mode I simulation. Details regarding the RVE and the material models used is given in the following section 4.

According to Matouš et al. (2008) the micro-to-macro transition is established by $\vec{t}^{Macro} = \langle\underline{\sigma}(\vec{x})\rangle_V \cdot \vec{n}$ for the macroscopic traction vector. The homogenization procedure including the scale transitions is summarized in Figure 1b.
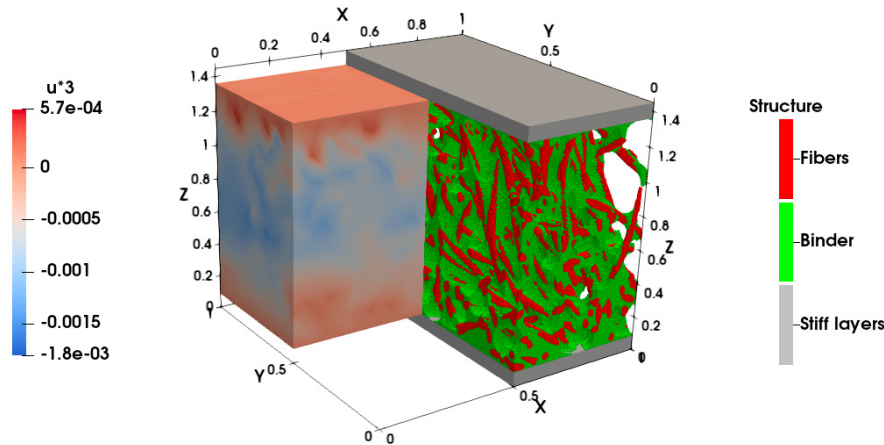
Fig. 2. Virtual RVE for Hybrix^{TM} core material and fluctuation displacement field under mode I loading.

4. Applications

Besides adhesive layers, Hybrix^{TM} sandwich plates represent an interesting application of the method. It is expected that the porous, polymeric fiber-binder core carries a negligible amount of in-plane loads in comparison to the metal face sheets and should consequently be well suited for CZM. Furthermore, it has a complex microstructure, which can be influenced by many production parameters, e.g., the fiber and binder volume fractions, the thickness and fiber geometry, as well as the materials used, which additionally makes it a promising candidate for virtual material development.

The virtual RVE for the core of the Hybrix^{TM} configuration investigated in this work is shown in Figure 3. The core has a thickness of 1.5 mm, whereas the face sheets of this configuration are 0.5 mm thick each. The fiber length is 2 mm and its diameter were determined as 50 μm from microscopy investigations. The volume fractions of fiber and binder are at about 13% and 22%, respectively, and they were obtained from microscopy and μCT investigations. Furthermore, the fiber orientation in the *xy*-plane is assumed to be arbitrary, whereas the distribution of the orientation with respect to the *z*-axis is modeled by a triangular-shaped function with its maximum at the arccosine of fiber length divided by the core thickness. The virtual RVE was then generated by setting the position, the orientation, and the curvature of the fibers s.t. the overlap of the fibers with one another and with the layer boundaries, as well as the deviation of the orientation with respect to the triangular distribution function and the curvature were as small as possible. The generated RVE is periodic in the *x*- and *y*-direction and stiff layers with a thickness of 0.1 mm each were added in *z*-direction.

The material parameters for the FFT simulations are summarized in Table 1. Young's modulus and yield stress of the perfect plastic von Mises model were obtained from microindentation experiments. It could thereby not be distinguished between the material parameters of fibers and binder, which is why we use the same model for both. The Poisson's ratio is estimated as a typical value for polymers.

Table 1. Material parameters used.

An example of a column heading	Youngs's modulus (*MPa*)	Poisson's ratio (-)	Yield stress (*MPa*)	p_{nl}^0 (-)	p_{nl}^f (-)
Fibers and binder	2330	0.4	90	0.15	0.8
Stiff layers	70000	0.33	-	-	-

The non-local damage initiation and failure parameters p_{nl}^0 and p_{nl}^f were determined from quasistatic, macroscopic reinforced DCB tests, which can be used to measure the mode I TSL. A scheme of the test is shown in Figure 3a. Hybrix^{TM} plates were bonded to steel adherents using an adhesive to reinforce the face sheets, and the tests were

performed at a rate of 30 μm/s at the load introduction points. The tests were evaluated with the *J*-integral (Rice (1968)), which is computed by

$$J = \frac{2F\theta}{b} \tag{8}$$

from the external load F, bending angle θ and the specimen width b, cf. Stigh et al. (2016). F and θ were measured with a load cell and a shaft encoder, respectively. The mode I component of the traction vector σ^I was then calculated by

$$\sigma^I = \frac{\mathrm{d}\,J}{\mathrm{d}\,u}, \tag{9}$$

whereby the mode I crack opening displacements u, which corresponds to the separation at the crack tip, was measured using LVDTs (Linear Voltage Differential Transformer). The test results are shown in Figure 3b.

The damage model parameters were then adjusted to fit the softening part of the measured TSL. It should be mentioned at this point, that the computational times for the FFT simulations are currently too high for an optimization method, which is why the parameters were manipulated manually until the softening parts roughly agree. The results of the FFT-based homogenization in mode I are shown in Figure 3b. The simulations did not fail at the end of the curve, but the computational time became unreasonable high and the simulations were aborted. Nevertheless, a good agreement between simulations and experiments, especially in elastic and plastic parts, of the TSL is shown.
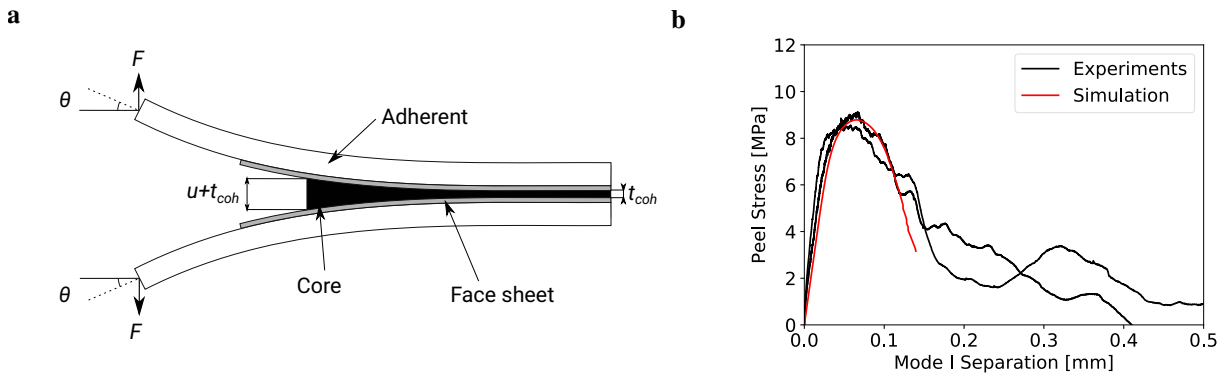

Fig. 3. (a) Scheme of the reinforced DCB test; (b) Comparison of results from FFT-based homogenization in mode I and reinforced DCB experiments.

5. Conclusions

A novel FFT-based homogenization scheme for Cohesive Zones was developed in this work. It exploits the expected reduced computational times of FFT-based homogenization methods in comparison to the existing FE-based methods. It could therefore allow for virtual material design processes for heterogeneous materials with complex microstructures that are modelled as finite thickness Cohesive Zones. The novel method was then applied to the core material of Hybrix^{TM} metal sandwich plates and the results were compared to experiments.

Nevertheless, there are still several uncertainties. First, the crack propagates in the in-plane direction of the Cohesive Zone and periodic boundary conditions are used there, which leads to cracks that are also periodic. In addition, gradient loads appear in the vicinity of a crack tip, which are also not considered. Despite these unrealistic assumptions, it was found in Kulkarni et al. (2010) that the results from their FE-based homogenization still agreed well with

results from a direct numerical simulation of the full heterogeneous layer in case of an adhesive. However, it still needs to be investigated how the method performs for different materials and where the limitations are. Moreover, the predictive capabilities regarding complex load cases and different microstructures should be evaluated in future work. Further comparisons with experimental results are especially necessary for this purpose.

In addition, the computational times can be rather high for some microstructures, such as the Hybrix^{TM} core material, with the current implementation of the solver on a workstation, whereas they are quite reasonable for adhesive layers. Therefore, a version of the solver for computer clusters is currently in progress and different algorithms could be tested in future work.

Finally, it should be mentioned that the results of the method should not depend on the size of the RVE used, if it has a constant thickness. This is usually not the case in standard computational homogenization continua, cf. Gitman et al. (2007).

Acknowledgements

References

Barzilai, J., Borwein, J.M., 1988. Two-point step size gradient methods. IMA Journal of Numerical Analysis 8(1), 141-148.

Bödeker, F., Marzi, S., 2020. Applicability of the mixed-mode controlled double cantilever beam test and related evaluation methods. Engineering Fracture Mechanics 235, 107149.

Frigo, M., Johnson, S.G., 2005. The Design and Implementation of FFTW3. Proceedings of the IEEE 93(2), 216–231.

Gitman, I.M., Askes, H., Sluysc, L.J., 2007. Representative volume: Existence and size determination. Engineering Fracture Mechanics 74(16), 2518–2534.

Kulkarni, M.G., Matouš, K., Geubelle, P.H., 2010. Coupled multi-scale cohesive modeling of failure in heterogeneous adhesives. Numerical Methods in Engineering 84(8), 916–946.

Lucarini, S., Segurado, J., 2019. On the accuracy of spectral solvers for micromechanics based fatigue modeling. Computational Mechanics 63, 365-382.

Magri, M., Lucarini, S., Lemoine, G., Adam, L., Segurado, J., 2021. An FFT framework for simulating non-local ductile failure in heterogeneous materials. Computer Methods in Applied Mechanics and Engineering 380, 113759.

Matouš, K., Kulkarni, M.G., Geubelle, P.H., 2008. Multiscale cohesive failure modeling of heterogeneous adhesives. Journal of the Mechanics and Physics of Solids 56(4), 1511–1533.

Matouš, K., Geers, M.G.D., Kouznetsova, V.G., Gillman, A., 2017. A review of predictive nonlinear theories for multiscale modeling of heterogeneous materials. Journal of Computational Physics 330, 192–220.

Menon, L., Dagum, R., 1998. OpenMP: An Industry-Standard API for Shared-Memory Programming. Computing in Science & Engineering v(01), 46–55.

Moulinec, H., Suquet, P., 1998. A numerical method for computing the overall response of nonlinear composites with complex microstructure. Computer Methods in Applied Mechanics and Engineering 157, 69–94.

Rice, J.R., 1968. A Path Independent Integral and the Approximate Analysis of Strain Concentration by Notches and Cracks. Journal of Applied Mechanics 35(2), 379–386.

Schneider, M., Ospald, F., Kabel, M., 2016. Computational homogenization of elasticity on a staggered grid. Numerical Methods in Engineering 105(9), 693–720.

Schneider, M., 2019. On the Barzilai-Borwein basic scheme in FFT-based computational homogenization. Numerical Methods in Engineering 118(8), 482–494.

Schneider, M., 2021. A review of nonlinear FFT-based computational homogenization methods. Acta Mechanica 232, 2051–2100.

Sharma, L., Peerlings, R.H.J., Shanthraj, P., Roters, F., Geers, M.G.D., 2018. FFT-based interface decohesion modelling by a nonlocal interphase. Advanced Modeling and Simulation in Engineering Sciences 5, 7.

Stigh, U., Biel, A., Svensson, D., 2016. Cohesive zone modelling and the fracture process of structural tape. Procedia Structural Integrity 2, 235–244.